Edge illumination X-ray phase contrast imaging with continuous mask motion

BEN HUYGE,[1,2,*] **NICHOLAS FRANCKEN,**[1,2] **JOAQUIM G. SANCTORUM,**[1,2] **JONATHAN SANCTORUM,**[1,2] **JAN DE BEENHOUWER,**[1,2] **AND JAN SIJBERS**[1,2]

[1]*imec - Vision Lab, Dept. of Physics, University of Antwerp, Universiteitsplein 1, 2610 Antwerp, Belgium*
[2]*DynXLab: Center for 4D Quantitative X-ray Imaging and Analysis, Universiteitsplein 1, 2610 Antwerp, Belgium*
[*]*ben.huyge@uantwerpen.be*

Abstract: Edge illumination (EI) is an X-ray phase contrast imaging technique in which two absorbing masks are employed. Sensitivity for attenuation, refraction, and dark field contrast is achieved by acquiring images while discretely stepping one mask parallel to the other. However, this step-and-shoot acquisition strategy results in dead time between the acquisition of each frame, thereby increasing the scan duration. Continuous acquisition provides several advantages over a conventional step-and-shoot acquisition, such as a shorter scan time and improved mechanical stability. In this paper, an EI imaging strategy is presented in which the mask is moved continuously during acquisition. We prove that the standard EI imaging model allows for an unbiased extraction of the contrasts from data acquired with continuous mask motion, even when the motion is not explicitly modeled. This is supported by simulated and experimental data, demonstrating that EI with continuous mask motion does not require modifications to the imaging model.

1. Introduction

Conventional X-ray computed tomography (CT) scans are performed with a step-and-shoot acquisition method, in which the sample remains stationary relative to the source during X-ray exposure [1]. Repositioning (e.g., translation or rotation) of the sample occurs between two exposures, resulting in dead times and consequently a long scan duration. Another drawback of the step-and-shoot acquisition method is its vulnerability to vibrations caused by repeated acceleration and deceleration of the components [2]. In contrast to step-and-shoot, continuous acquisition is a technique where the sample is moved uninterruptedly during X-ray exposure. Hence, all projections are acquired without dead times, thereby substantially reducing the scan duration [3]. While continuously moving the sample during exposure may lead to artefacts in the reconstructed image due to motion blur, various techniques have been proposed to mitigate this problem [4–8]. The concept of continuous acquisition can be extended to X-ray phase contrast imaging techniques, such as edge illumination, which suffer from even longer acquisition times compared to conventional X-ray imaging. However, to our knowledge, a method for continuous edge illumination phase contrast imaging does not yet exist.

In edge illumination (EI) phase contrast imaging, two absorbing masks with parallel aperture slits are employed: a sample mask, which divides the X-ray beam into separate so-called beamlets, and a detector mask, which is positioned close to the detector so that it creates insensitive regions between adjacent pixels [9–11]. Masks have also been designed with different aperture shapes to enable phase sensitivity in two directions [12,13]. By discretely stepping the sample mask parallel to the detector mask, each beamlet shifts over the exposed center of a detector pixel, thereby sampling the so-called illumination curve (IC). From the sampled IC, three complementary image contrasts can then be derived: attenuation, refraction and dark field. The IC sampling can

be time consuming, especially for EI computed tomography (EI-CT) scans, because multiple images according to the different mask positions need to be acquired for each rotation angle. Additionally, a step-and-shoot scan suffers from dead time between consecutive acquisitions due to the repositioning of the mask, causing EI-CT to be even more time consuming [14]. Also, the repeating start and stop motions of a step-and-shoot acquisition can cause unwanted displacement of the mask during the scan, resulting in image artefacts [15]. These drawbacks limit practical applications such as high throughput scanning and the scanning of dynamic processes [16].

The implementation of continuous mask motion enables a more time efficient and stable acquisition for standard EI. A similar approach has been proposed for grating-based interferometry, a different phase contrast imaging technique where the gratings have a smaller period and aperture width compared to the masks in EI [17–19]. Continuous motion of the grating has been performed to reduce both acquisition time and mechanical instabilities. However, to our best knowledge, this approach is unexplored for EI.

In this paper, we propose an EI acquisition protocol with continuous sample mask motion during acquisition. We show that the standard IC model correctly retrieves the attenuation, refraction and dark field contrast by demonstrating that the effects of the motion are eliminated by flat field correction. We validate our theoretical findings both with simulated and experimental data.

2. Methods

2.1. Edge illumination

EI relies on two absorbing masks: a sample mask, positioned between the source and the sample, and a detector mask positioned right in front of the detector. The sample mask splits the X-ray beam into multiple smaller beams called beamlets, in such a way that each pixel is illuminated by a beamlet, as shown in Fig. 1. The detector mask covers the area between neighboring pixels to create insensitive regions between them, while leaving their central regions exposed.
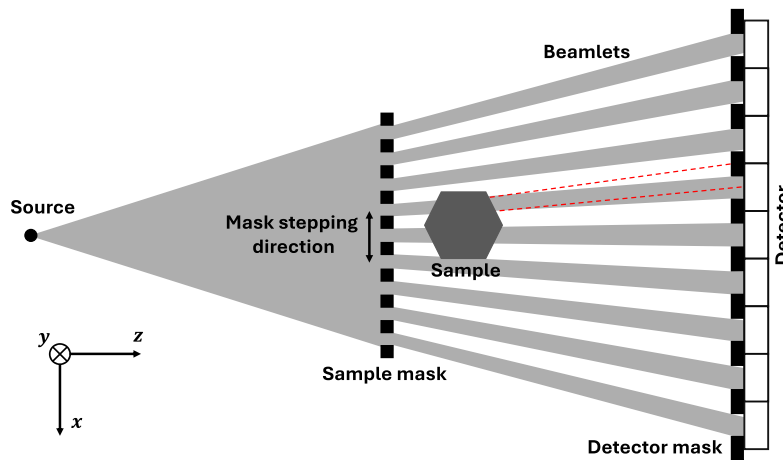

Fig. 1. Top-down illustration of an EI setup (not to scale). The red dashed lines show the effect of refraction and broadening of a beamlet, resulting in a change in measured intensity in the pixel.

In EI, the sample mask is stepped laterally with respect to the detector mask. This change in mask position causes a shift of the beamlet on each detector pixel, changing the illuminated area. The function that relates the measured intensity in a detector pixel to the mask position is called the illumination curve (IC), which typically assumes a near-Gaussian shape due to system blur

and convolution of the finite source intensity profile with the sample and detector mask apertures [20]. The IC is sampled by acquiring images at different sample mask positions. Interactions between the X-rays and the sample, such as absorption, refraction, and scatter, will influence the IC. Hence, for each pixel, the contrasts can be extracted by comparing the differences between the IC with and without the sample in the X-ray beam [21].

The IC, describing the intensity as a function of the sample mask position x, is usually modelled as a Gaussian function [22]:

$$I(x) = a \exp\left(-\frac{(x-b)^2}{2c^2}\right) + d, \tag{1}$$

where a is the amplitude, b the peak position, c^2 the variance, and d the offset. The sample mask position x is zero when both masks are aligned and is positive or negative depending on the direction of the sample mask shift (cf. Fig. 1). The contrasts are calculated from the parameters a, b and c^2 of the Gaussian IC model. In practice, X-ray transmission through the masks can result in an offset of the IC, which may lead to a bias in the estimated height and width of the IC [22]. To account for this, the offset d is included in the Gaussian model, allowing for a correct estimation of the contrast parameters a, b and c^2. As the IC model contains four parameters, the IC must be sampled at least at four different mask positions to extract the contrasts and the offset of the Gaussian. The total attenuation μ_{tot} is related to the change in area under the IC with and without the sample in the beam. The refraction contrast yields the refraction angle of the X-rays and is calculated from the shift of the IC peak position. The dark field contrast arises from small angle X-ray scattering from micro-structures smaller than the aperture width and is extracted from the broadening of the IC [23,24]. Sharp sample edges can also yield dark field contrast if they are unresolved [25]. Specifically, the total attenuation μ_{tot}, refraction angle α and dark field σ^2 (angular broadening) are calculated as follows [26]:

$$\mu_{tot} = -\ln\left(\frac{ac}{a_f c_f}\right), \tag{2}$$

$$\alpha = \frac{m}{z_{od}}(b - b_f), \tag{3}$$

$$\sigma^2 = \frac{m^2}{z_{od}^2}(c^2 - c_f^2). \tag{4}$$

Here, m is the magnification factor and z_{od} is the distance between the object and the detector. The subscript f denotes the parameter estimated from the flat field IC (i.e. without the sample in the beam).

2.2. Edge illumination with continuous mask motion

The purpose of this section is to theoretically prove that the standard Gaussian model (Eq. 1) can be used to correctly extract the contrasts from a scan with continuous mask motion. To prove this, in 2.2.1, we first develop a model for the IC that explicitly takes the mask motion into account, allowing an unbiased estimation of the IC parameters. Then, in 2.2.2, we use that model to show that flat field normalization removes the bias caused by continuous mask motion, so that the contrasts are unbiased, even when extracted by fitting the standard step-and-shoot Gaussian IC.

2.2.1. Incorporating mask motion in the IC model

In Eq. (1), the sample mask position x is fixed during the acquisition of each projection. However, when the sample mask moves continuously, the beamlets shift over the pixel while the intensity is measured. To account for this effect, the model in Eq. (1) can be adapted by integrating the

IC between two mask positions $x - vt/2$ and $x + vt/2$, where vt is the size of the integration interval, with v the translation speed of the sample mask and t the acquisition time. We assume the translation speed of the mask to be known and constant during acquisition. The model for the IC with continuous mask motion can be written as:

$$I_m(x) = \frac{1}{vt} \int_{x-\frac{vt}{2}}^{x+\frac{vt}{2}} \left(a \exp\left(-\frac{(\xi - b)^2}{2c^2}\right) + d \right) d\xi, \tag{5}$$

where x denotes the center of the integration interval, along the mask stepping axis (cf.Fig. 1). The integration in Eq. (5) yields the following expression for the modified IC:

$$I_m(x) = \frac{a}{vt} \sqrt{\frac{\pi c^2}{2}} \left(\text{erf}\left(\frac{x + \frac{vt}{2} - b}{\sqrt{2c^2}}\right) - \text{erf}\left(\frac{x - \frac{vt}{2} - b}{\sqrt{2c^2}}\right) \right) + d, \tag{6}$$

where erf(.) denotes the error function [27]. For brevity, we will refer to the step-and-shoot Gaussian IC model as the static model (Eq. (1)) and to the IC model with continuous sample mask motion as the motion model (Eq. (6)). By fitting the motion model to the measured intensities, the parameters a, b, c^2 and d can be estimated, from which the contrasts are derived according to Eqs. (2) to (4). For the derivation of the motion model, we assumed that the static model is Gaussian shaped [20,21].

The continuous mask motion results in a decrease of the amplitude a and an increase of the variance c^2, due to the averaging of measured intensities around the peak and tails of the Gaussian, respectively. This causes a bias in the parameter estimation, which is accounted for by the motion model by explicitly incorporating the continuous mask motion.

While Eq. (6) explicitly accounts for continuous mask motion, we will show in 2.2.2 that this motion model is not required to extract the different contrasts and that the standard static model can still be used. This is because the bias introduced by using the static model is also present in the flat field and can hence be eliminated by flat field normalization.

2.2.2. Contrast retrieval with continuous mask motion

In this section, we use the motion model to theoretically show that the static model can also be used to correctly extract the contrasts from a scan with continuous mask motion, even though the static model does not assume sample mask motion. We do this by first expressing the contrasts in terms of the moments of the IC [28,29]. The nth-order moment of an arbitrary function $g(z)$ is defined as [30]:

$$M_n(g) = \int z^n g(z) dz. \tag{7}$$

The attenuation contrast, given by Eq. (2), is calculated by taking the negative logarithm of the ratio between the area under the sample IC and the flat field IC. As shown by Eq. (7), the area under the IC corresponds to the 0th-order moment of the IC, so Eq. (2) can be written as

$$\mu_{tot} = -\ln\left(\frac{ac}{a_f c_f}\right) = -\ln\left(\frac{M_0(I)}{M_0(I_f)}\right), \tag{8}$$

where I is the IC of the sample and I_f the IC of the flat field.

The refraction contrast is proportional to the difference of the peak position between the sample IC and flat field IC, as defined in Eq. (3). The peak position is given by the 1st-order moment of the IC, normalized by the 0th-order moment because the area under the IC is not 1 [31]. Hence, Eq. (3) can be written as

$$\alpha = \frac{m}{z_{od}}(b - b_f) = \frac{m}{z_{od}} \left(\frac{M_1(I)}{M_0(I)} - \frac{M_1(I_f)}{M_0(I_f)} \right). \tag{9}$$

The dark field contrast is proportional to the difference in variance between the sample IC and flat field IC (Eq. (4)). This can be represented with the 2nd-order normalized and centralized

moment of the IC [29], so that Eq. (4) can be written as

$$\sigma^2 = \frac{m^2}{z_{od}^2}(c^2 - c_f^2) = \frac{m^2}{z_{od}^2}\left(\frac{M_2(I)}{M_0(I)} - \frac{M_1^2(I)}{M_0^2(I)} - \left(\frac{M_2(I_f)}{M_0(I_f)} - \frac{M_1^2(I_f)}{M_0^2(I_f)}\right)\right). \tag{10}$$

Having expressed all three contrasts as moments of the IC, the next step is to describe the blurring of the IC in the motion model (Eq. (5)) as a convolution of the static IC model with a rectangular function,

$$I_m(x) = (I * R)(x) = \int_{-\infty}^{\infty} I(\xi)R(x - \xi)d\xi. \tag{11}$$

Here, $I(\xi)$ is the static IC model from Eq. (1) and $R(x)$ is a rectangular function defined by

$$R(x) = \frac{1}{vt}\text{Rect}\left(\frac{x}{vt}\right), \tag{12}$$

where $\text{Rect}(x/vt)$ equals 0 everywhere, except for $|x| \leq vt/2$, where it equals 1. Integrating Eq. (11) results in the same expression as the motion model in Eq. (5). Subsequently, the following identities describing the moments of a convolution of two functions g and h are used [32]:

$$M_0(g * h) = M_0(g)M_0(h), \tag{13}$$

$$M_1(g * h) = M_0(g)M_1(h) + M_1(g)M_0(h), \tag{14}$$

$$M_2(g * h) = M_0(g)M_2(h) + M_2(g)M_0(h) + 2M_1(g)M_1(h). \tag{15}$$

First, to prove that continuous sample mask motion during acquisition has no effect on the retrieved attenuation, the motion model is substituted in Eq. (8),

$$\mu_{tot} = -\ln\left(\frac{M_0(I_m)}{M_0(I_{m,f})}\right) = -\ln\left(\frac{M_0(I * R)}{M_0(I_f * R)}\right), \tag{16}$$

where the subscript m denotes the motion IC model (Eq. (11)) and the subscript f denotes the flat field of that IC. By using the identity in Eq. (13), it follows that

$$\mu_{tot} = -\ln\left(\frac{M_0(I)M_0(R)}{M_0(I_f)M_0(R)}\right) = -\ln\left(\frac{M_0(I)}{M_0(I_f)}\right) = -\ln\left(\frac{ac}{a_f c_f}\right), \tag{17}$$

with $M_0(R) = 1$ the area under the rectangular function $R(x)$. Eq. (17) is identical to Eq. (2), showing that the expression for the attenuation contrast remains unchanged if continuous sample mask motion during acquisition is employed.

A similar result can be obtained for the refraction contrast by following the same approach. The motion model is substituted in Eq. (9), yielding

$$\alpha = \frac{m}{z_{od}}\left(\frac{M_1(I * R)}{M_0(I * R)} - \frac{M_1(I_f * R)}{M_0(I_f * R)}\right). \tag{18}$$

Using the identities in Eqs. (13) and (14), with $M_1(R) = 0$, because the rectangular function $R(x)$ is symmetric, it follows that

$$\alpha = \frac{m}{z_{od}}\left(\frac{M_1(I)}{M_0(I)} - \frac{M_1(I_f)}{M_0(I_f)}\right) = \frac{m}{z_{od}}(b - b_f), \tag{19}$$

which is identical to Eq. (3), showing that the refraction contrast is also unchanged by the continuous mask motion.

Finally, for the dark field contrast, the IC model with continuous mask motion is substituted in 10 and the identities from Eqs. (13) and (14) are applied, resulting in

$$\sigma^2 = \frac{m^2}{z_{od}^2} \left(\frac{M_2(I * R)}{M_0(I)M_0(R)} - \frac{M_1^2(I)}{M_0^2(I)} - \left(\frac{M_2(I_f * R)}{M_0(I_f)M_0(R)} - \frac{M_1^2(I_f)}{M_0^2(I_f)} \right) \right). \tag{20}$$

Then, applying the identity from Eq. (15) yields:

$$\sigma^2 = \frac{m^2}{z_{od}^2} \left(M_2(R) + \frac{M_2(I)}{M_0(I)} - \frac{M_1^2(I)}{M_0^2(I)} - \left(M_2(R) + \frac{M_2(I_f)}{M_0(I_f)} - \frac{M_1^2(I_f)}{M_0^2(I_f)} \right) \right) \tag{21}$$

$$= \frac{m^2}{z_{od}^2} \left(\frac{M_2(I)}{M_0(I)} - \frac{M_1^2(I)}{M_0^2(I)} - \left(\frac{M_2(I_f)}{M_0(I_f)} - \frac{M_1^2(I_f)}{M_0^2(I_f)} \right) \right) = \frac{m^2}{z_{od}^2}(c^2 - c_f^2). \tag{22}$$

Equation (22) is identical to Eq. (4), showing that even the dark field contrast is unaffected by continuous motion during acquisition.

Equations (17), (19) and (22) demonstrate that the same attenuation, refraction, and dark field contrast obtained with conventional step-and-shoot scanning, can also be obtained if the sample mask is continuously shifted during acquisition, without modifications to the IC model. This result is key to continuous EI-CT since it opens up the possibility of a more mechanically stable and faster continuous acquisition mode.

3. Experiments

3.1. Simulation experiments

Simulation experiments were performed with GATE [33,34], a Monte Carlo based framework layered on top of GEANT4 [35]. Furthermore, necessary tools for phase contrast imaging in GATE were employed [36]. In the simulation, the source emitted a fan beam of monochromatic X-rays with an energy of 25 keV and had a uniform line focal spot of 50 μm. The detector consisted of a row of 100 pixels, each with a size of 150 μm, positioned 900 mm from the source. The sample mask was placed at a distance of 600 mm from the source and had an aperture width of 20 μm, a period of 100 μm and a thickness of 225 μm. The detector mask was placed 12 mm in front of the detector and had an aperture width of 30 μm, a period of 148 μm and a thickness of 225 μm. Both masks were modeled as fully impenetrable to eliminate X-ray transmission through
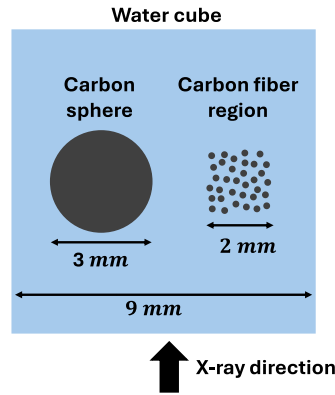

Fig. 2. Illustration of the phantom used in the simulations. The diameters of the carbon fibers are not to scale.

the masks. The phantom was placed 13 mm behind the sample mask, and had a magnification factor of $m = 1.47$ with an object-detector distance of $z_{od} = 287$ mm. The phantom consisted of a cube of water with a side of 9 mm, in which a homogeneous carbon sphere with a diameter of 3 mm and a cubic region with a side of 2 mm were placed. The cubic region was filled with 17080 parallel carbon fibers, each with a radius of 3 μm. The phantom is shown in Fig. 2.

First, a step-and-shoot simulation was performed with five mask steps of 7.2 μm, in a range of [−14.4 μm, 14.4 μm], where 0 μm corresponds to the position where the sample mask aligns with the detector mask. Next, a simulation with 700 mask steps of approximately 0.05 μm was performed, covering a range of [−18 μm, 18 μm]. The purpose was to simulate continuous mask motion during acquisition. This was done by averaging the 700 mask steps of each IC in groups of 140 adjacent steps, resulting in ICs sampled with 5 mask steps, where each step contains the integrated intensity over an interval of 7.2 μm. To ensure a fair comparison between both simulated scans, the step-and-shoot scan was repeated 140 times ($5 \cdot 140 = 700$) and the data was averaged over the repetitions before fitting the IC, to achieve a similar signal to noise ratio compared to the continuous scan. Because the masks were modeled as fully absorbing, the offset parameter d from the models in Eqs. (1) and (6) was fixed to 0 for the simulated data.

3.2. Real experiments

Experimental data was acquired with the FleXCT scanner [37]. To enable EI experiments, the scanner was equipped with two absorbing masks, made of gold on a graphite substrate [38]. The sample mask had a period of 100 μm, an aperture width of 20 μm, a thickness of 225 μm and was positioned at a distance of 650 mm from the source. The detector mask had a period of 148 μm, an aperture of 30 μm, a thickness of 225 μm and was placed 962 mm from the source. The sample mask was mounted on a PI H-811.I2 6-Axis Miniature Hexapod to perform the discrete mask stepping and continuous motion. Before the scan, the sample and detector mask were aligned according to the procedures discussed in [39,40].

The distance between the source and the detector was 975 mm, the tube voltage was set to 40 kV, with a power of 60 W and the exposure time was set to 2 s. The pixels of the detector had a size of 150 μm. The object was a piece of tree branch that was placed in the X-ray beam at a distance of 700 mm from the source, with a magnification factor of 1.39.

First, the object was imaged at 19 different mask positions distributed equally over a range of [−45 μm, 45 μm], in a step-and-shoot acquisition. This scan is the reference step-and-shoot-scan. Then, a scan was performed with continuous mask motion, covering the same range of [−45 μm, 45 μm]. This total range was divided in 5 acquisition intervals of 18 μm, over which the intensity was integrated. The speed of the hexapod was 9 μm s^{-1}. The stepping range was divided in 5 intervals to maximize the size of the integration interval, while ensuring sufficient sample points for accurate IC fitting. A subset of 5 mask positions was selected from the reference step-and-shoot data to compare the data with continuous motion to step-and-shoot data with the same number of IC points. The 5 mask steps were distributed equally over a range of [−30 μm, 30 μm].

In our experiments, acceleration of the hexapod at the start and end of the continuous mask motion was quasi-instantaneous for this slow speed and, as a result, the duration of acceleration was considered negligible compared to the long exposure time of 2s. For both the simulations and the experiments, the IC curve fitting was performed with the non-linear least squares method provided by the SciPy *curve_fit* function [41].

4. Results and discussion

4.1. Simulation experiments

The amplitude, peak position, and variance extracted from the sample ICs of the different simulations are shown in Fig. 3. These parameters are shown in black when extracted from the sample ICs of the reference step-and-shoot simulation (with static model). The parameters from the simulation with continuous sample mask motion are shown in orange when extracted with the static model (Eq. (1)) and in blue when extracted with the motion model (Eq. (6)).
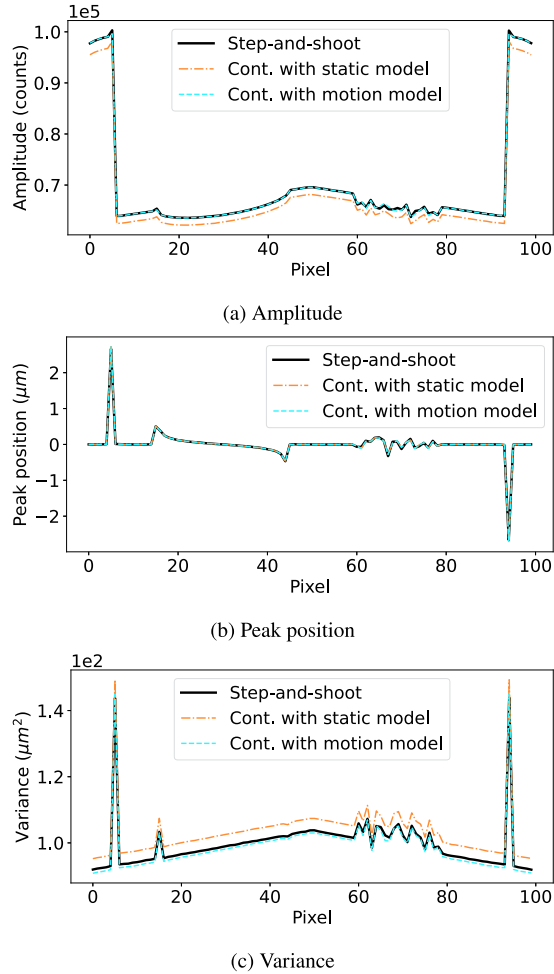

(a) Amplitude

(b) Peak position

(c) Variance

Fig. 3. The sample IC amplitude (a), peak position (b) and variance (c) for the step-and-shoot simulation, the simulation with continuous mask motion extracted with the static model (Eq. (1)) and extracted with the motion model (Eq. (6)).

In Fig. 3(a), it can be observed that the IC amplitude from the scan with continuous sample mask motion, extracted by fitting the static IC model, is notably lower than the amplitude of the reference step-and-shoot scan. However, no difference can be observed in the IC peak positions of the different scans shown in Fig. 3(b). Finally, Fig. 3(c) shows that the variance from the scan with continuous mask motion, extracted with the static IC model, is overestimated.

These observations are in line with the expectations set in 2.2.1. Averaging the intensity around the peak of the IC results in a decrease of the amplitude. Similarly, averaging in the tails of the

IC has a broadening effect, increasing the variance. Continuous mask motion during acquisition does not influence the peak position of the IC. This follows from Eq. (11), since convolving a Gaussian IC with a symmetric rectangular function does not shift the peak position.

In Fig. 3, it can also be observed that the amplitude and variance, extracted by fitting the motion model to the data acquired with continuous mask motion (blue line), correspond substantially better to the reference step-and-shoot simulation, compared to the parameters extracted by fitting the static model to the continuous data (orange line). This demonstrates that the motion model eliminates the bias in the amplitude and variance estimation from data acquired with continuous sample mask motion. Whereas the variance estimated with the static model is 3.62% higher than the variance from the step-and-shoot scan, the variance estimated with the motion model is on average only 0.85% lower. The slight discrepancy between the variances obtained via step-and-shoot and continuous motion can be attributed to the nature of the simulations, as they produced idealized beamlet shapes which are not necessarily perfectly Gaussian. This introduces a subtle mismatch between model and data, which is less pronounced in the case of the continuous motion, as the introduced blurring results in an increased smoothing of the beamlet profile.
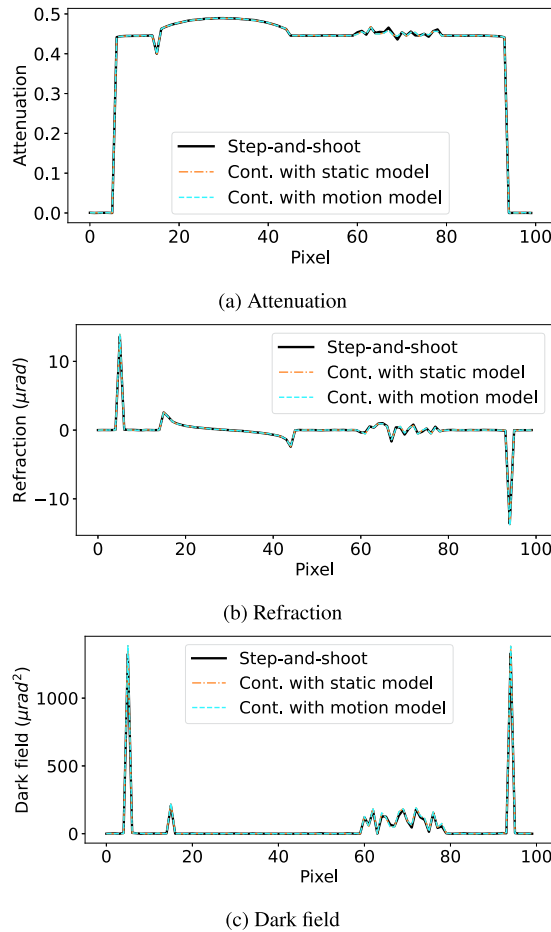

(a) Attenuation

(b) Refraction

(c) Dark field

Fig. 4. The attenuation (a), refraction (b) and dark field contrast (c) of the step-and-shoot simulation, the simulation with continuous mask motion extracted with the static model (Eq. (1)) and extracted with the motion model (Eq. (6)).
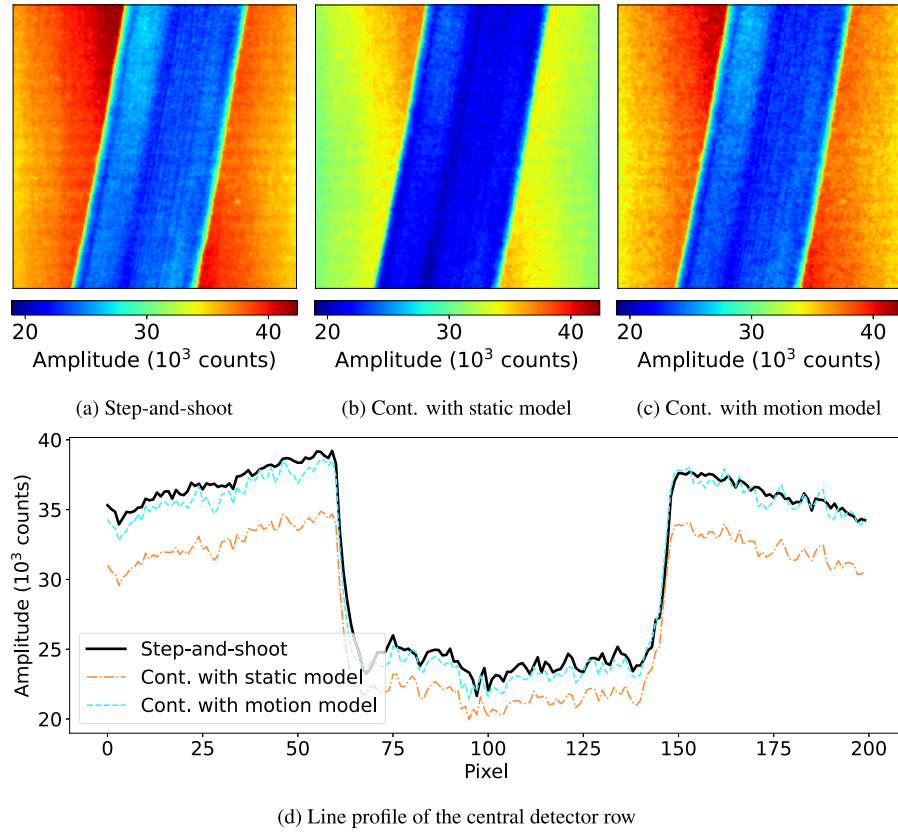
(a) Step-and-shoot   (b) Cont. with static model   (c) Cont. with motion model

(d) Line profile of the central detector row

Fig. 5. The amplitude of the sample ICs from the reference step-and-shoot scan (a), the scan with continuous mask motion with static model (Eq. (1)) (b) and with the motion model (Eq. (6)) (c). The profiles from the central detector row are shown in (d).

The attenuation, refraction, and dark field contrasts were obtained from the IC parameters via Eqs. (2) to (4) and are shown in Fig. 4. The contrasts obtained from the reference step-and-shoot simulation are shown in black. The contrasts from the simulations with continuous sample mask motion are shown in orange if extracted with the static model (Eq. (1)) and in blue if extracted with the motion model (Eq. (6)). In Fig. 4, a dip and peak can be observed in the attenuation and dark field, respectively, on the left side of the carbon sphere. This artefact is caused by the beamlet entering the sphere while stepping the IC, which breaks the Gaussian form and results in an erroneous parameter estimation. As shown in Fig. 4, there is no observable difference in the retrieved contrasts. Following the derivation in Section 2.2.2, the continuous sample mask motion during acquisition does indeed not influence the retrieved contrasts.

4.2. Real experiments

Figure 5 shows the amplitude of the sample ICs extracted from the reference step-and-shoot scan (Fig. 5(a)), the scan with continuous sample mask motion using the static model (Fig. 5(b)) and the scan with continuous sample mask motion using the motion model (Fig. 5(c)). Figure 5(d) shows the profile from the central detector row of these images. In a similar way, Figs. 6 and 7 show the peak position and variance of the sample ICs, respectively. A comparison between the parameters extracted from the data with continuous mask motion and the step-and-shoot scan with 5 mask steps can be found in the Supplement 1 (Fig. S1 to S3). The RMSE is calculated for

the images obtained via the static model and motion model by comparing them with the reference step-and-shoot image, and the values are shown in 1. The RMSE of the step-and-shoot scan with 5 mask steps is also calculated by comparing it with the reference step-and-shoot scan.

Table 1. The RMSE of the images (Figs. 5 to 7) obtained via the static model (Eq. (1)) and motion model (Eq. (6)) by comparing them with the reference step-and-shoot image. The RMSE of the step-and-shoot scan with 5 mask steps is also calculated by comparing it with the reference step-and-shoot scan

	Step-and-shoot (5 steps)	Static model	Motion model
Amplitude	397	3683	915
Peak position	0.11	0.19	0.19
Variance	3.7	25.7	7.3

In Fig. 5, it can be observed that the amplitude, extracted from the scan with continuous mask motion by fitting the static model, is lower compared to the reference. In Fig. 6 there is no visible difference in IC peak position between the different models and in Fig. 7 it can be seen that the variance of the scan with continuous mask motion and extracted with static model is overestimated compared to the reference variance. These observations are in agreement with the simulated data and show that the motion model eliminates the bias in the amplitude and variance estimations.
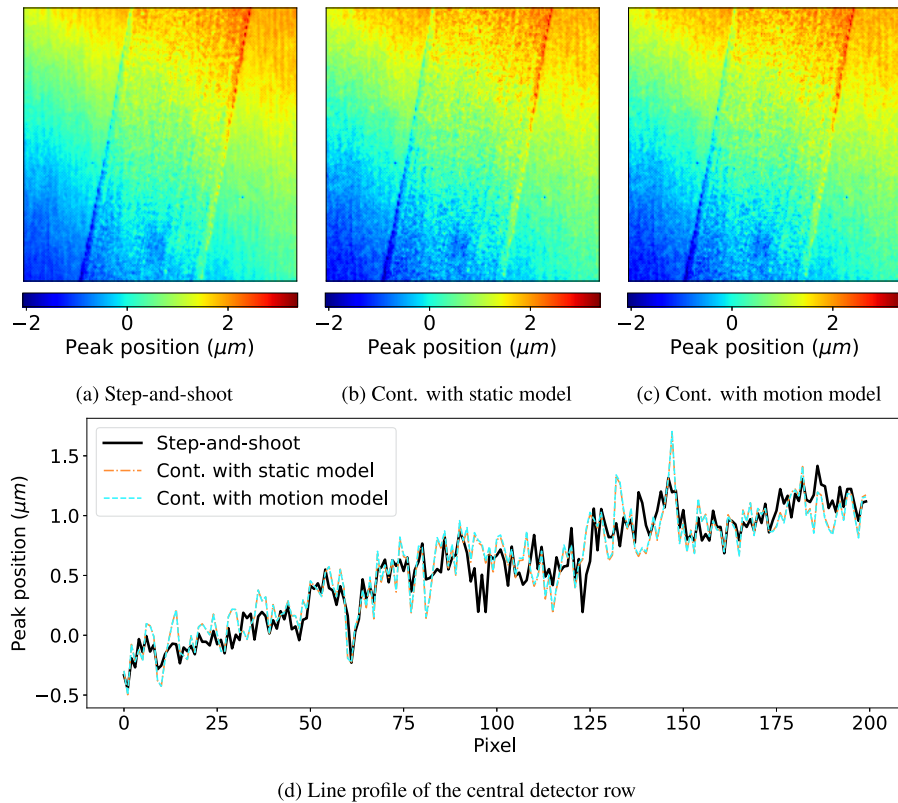

(a) Step-and-shoot   (b) Cont. with static model   (c) Cont. with motion model

(d) Line profile of the central detector row

Fig. 6. The peak position of the sample ICs from the reference step-and-shoot scan (a), the scan with continuous mask motion with static model (Eq. (1)) (b) and with the motion model (Eq. (6)) (c). The profiles from the central detector row are shown in (d).

(a) Step-and-shoot   (b) Cont. with static model   (c) Cont. with motion model

(d) Line profile of the central detector row

Fig. 7. The variance of the sample ICs from the reference step-and-shoot scan (a), the scan with continuous mask motion with static model (Eq. (1)) (b) and with the motion model (Eq. (6)) (c). The profiles from the central detector row are shown in (d).
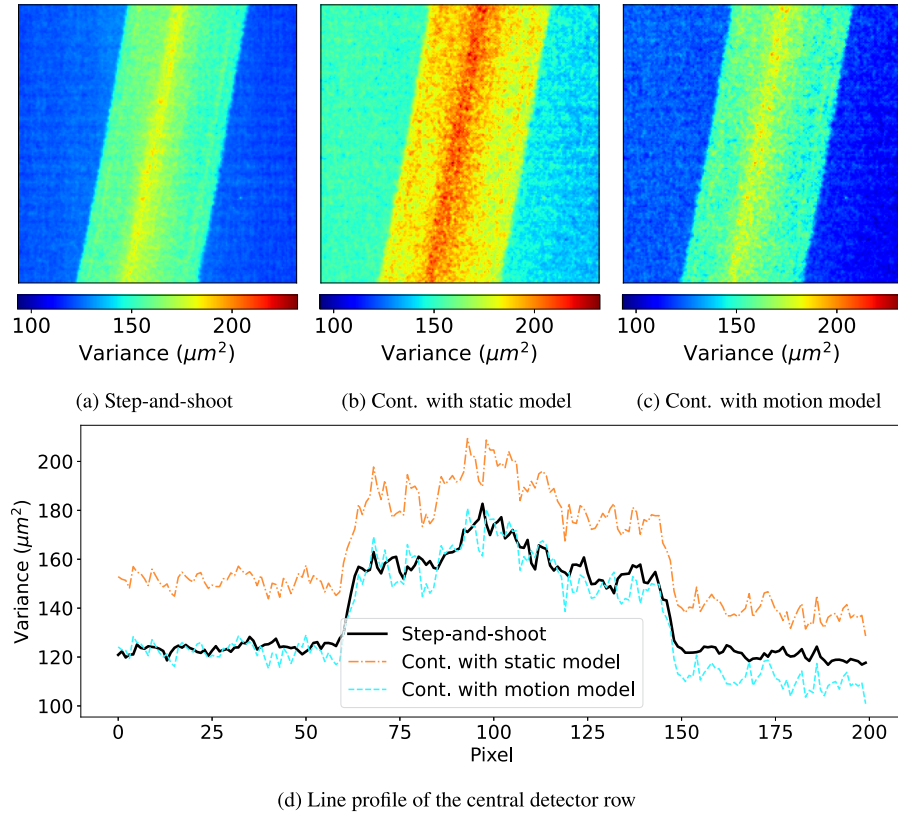
A difference compared to the simulated data is that a shift in IC peak position was observed in the background of the projections and their respective flat fields. This is attributed to mechanical instabilities of the setup that cause the sample mask to slightly shift between scans. The peak positions were corrected by calculating the average position of an area in the background of each image and subtracting this value from the image. The shifting of the IC peak position over repeated scans is a known challenge in EI and can be corrected with a post processing algorithm such as the one in [15]. However, this correction algorithm was designed for Gaussian ICs. Its application to scans with continuous mask motion will be subject to further study.

Finally, the attenuation, refraction and dark field contrast images for the different scans are shown in Fig. 8, where it can be observed that the contrasts extracted from the step-and-shoot scan with 19 mask steps are less noisy compared to the contrasts extracted with the motion model. This might give the impression that the motion model leads to noisier images. However, when compared with the step-and-shoot scan with 5 mask positions, a similar noise level is observed. Hence, the lower noise in the contrasts extracted from the step-and-shoot scan with 19 mask steps is the result of a denser IC sampling, compared to only 5 points for the scan with continuous mask motion.

The profiles from the central detector row of the attenuation, refraction and dark field images in Fig. 8 are shown in Fig. 9, compared with the reference step-and-shoot scan. Here, it is also observed that the contrasts from the scan with continuous motion are quasi-identical to the
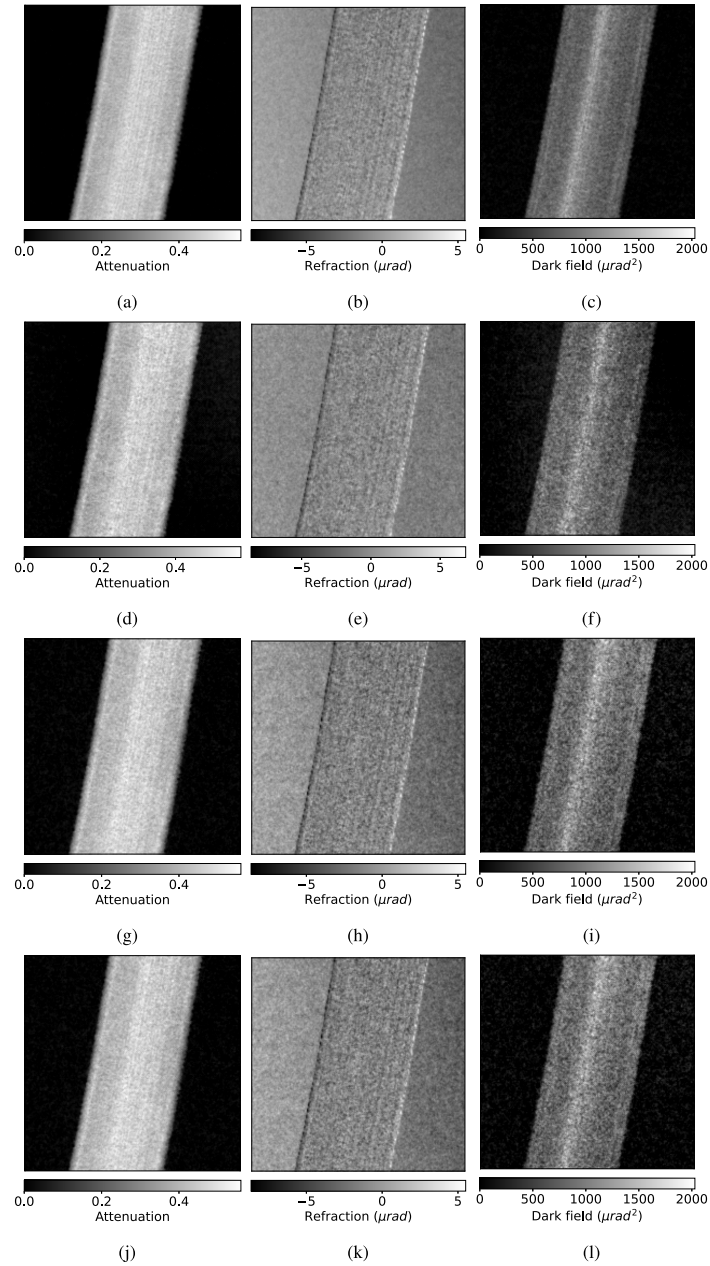
Fig. 8. The contrasts from the reference step-and-shoot scan (a-c); step-and-shoot scan with 5 mask steps (d-f) and the scan with continuous mask motion, extracted with the static model (g-i) and extracted with the motion model (j-l).

reference, irrespective of which IC model is used, substantiating the theoretical proof in Section 2.2.2. The profiles from the central detector row of the attenuation, refraction and dark field images, compared with the step-and-shoot scan with 5 mask steps, are shown in the Supplement 1 (Fig. S4).

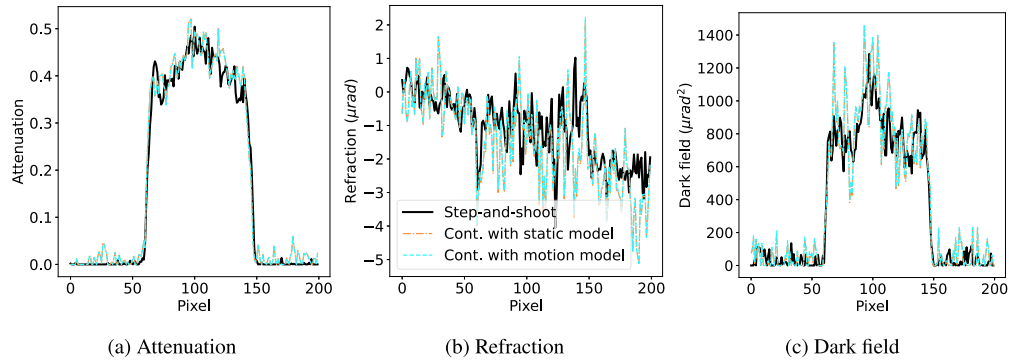|(a) Attenuation|(b) Refraction|(c) Dark field|

Fig. 9. The profiles from the central detector rows of the attenuation (a), refraction (b) and dark field (c) images, where the profile from the reference step-and-shoot scan is shown in black. For the scan with continuous mask motion, the profile is shown in orange when extracted with the static model (Eq. (1)) and in blue when extracted with the motion model (Eq. (6)).

The presented results demonstrate that it is possible to perform continuous mask motion during acquisition and correctly extract the contrasts without modifications to the Gaussian IC model, because the flat field correction eliminates the bias in the parameter estimation. However, this will not work when the mask motion in the flat fields is not identical to the projections. For example, when the flat field is acquired with step-and-shoot while the projections are continuously acquired. In that case, the static (Gaussian) model should be used to extract the parameters from the flat field and the motion model should be used for the continuous data to avoid the estimation bias and to ensure a correct contrast retrieval.

The motion model also assumes that the motion of the sample mask is constant during the acquisition time. Depending on the motors in the experimental setup, this might be challenging to achieve due to mask acceleration and deceleration at the beginning and end of the IC sampling.

The acquisition strategy of continuous mask motion can be combined with continuous rotation to enable efficient EI-CT scanning. An image reconstruction method would need to be developed that takes into account the continuous rotation of the object in combination with the continuous translation of the sample mask to reconstruct the different contrasts without blurring artefacts. In addition, this could also be combined with dithering, a process to increase the spatial resolution beyond the demagnified pixel size by translating the object in small (sub-pixel size) steps [42,43]. Data sparsity will be a major challenge for the combination of these different motions, because projections cannot be acquired for every rotation angle, dithering step and sample mask position. Finally, depending on the available EI-CT hardware, continuous scanning may lead to a significant gain in scan speed. Indeed, Hagen et al. reported a dead time of 0.8 s per projection, which amounts to a large part of the total scan time when measuring thousands of projections [14].

5. Conclusion

In this paper, we proposed an EI imaging strategy with continuous sample mask motion. We demonstrated that fitting a conventional Gaussian IC model to EI X-ray data that was acquired with continuous sample mask motion still yields accurate attenuation, refraction, and dark field contrast estimates, even when the continuous motion was not explicitly modelled. Specifically, by developing an IC model that explicitly incorporates continuous mask motion, it has been mathematically shown that flat field correction leads to the same attenuation, refraction, and dark field contrast as obtained from using a conventional model without explicit motion modelling.

Future work includes research on cases where the motion IC model provides improvements in the contrasts over the standard Gaussian model, which can occur if the flat fields do not fully compensate for the motion. Finally, continuous object rotation should be included with continuous sample mask motion to perform an EI-CT scan.

Disclosures. The authors declare no conflicts of interest.

Data availability. Data underlying the results presented in this paper are not publicly available at this time but may be obtained from the authors upon reasonable request.

Supplemental document. See Supplement 1 for supporting content.

References

1. W. A. Kalender, "X-ray computed tomography," Phys. Med. Biol. **51**(13), R29–R43 (2006).
2. M. O. Jousi, J. Erkkilä, M. Varjonen, *et al.*, "A new breast tomosynthesis imaging method: Continuous sync-and-shoot - technical feasibility and initial experience," Acta Radiol. Open **8**(3), 2058460119836255 (2019).
3. H. U. Kerl, C. T. Isaza, H. Boll, *et al.*, "Evaluation of a continuous-rotation, high-speed scanning protocol for micro-computed tomography," J. Comput. Assist. Tomogr. **35**(4), 517–523 (2011).
4. J. Cant, W. J. Palenstijn, G. Behiels, *et al.*, "Modeling blurring effects due to continuous gantry rotation: Application to region of interest tomography," Med. Phys. **42**(5), 2709–2717 (2015).
5. D. Chen, H. Li, Q. Wang, *et al.*, "Computed tomography for high-speed rotation object," Opt. Express **23**(10), 13423 (2015).
6. J. Zhang, W.-K. Lee, and M. Ge, "Sub-10 second fly-scan nano-tomography using machine learning," Commun. Mater. **3**(1), 91 (2022).
7. S. Majee, S. Aslan, D. Gürsoy, *et al.*, "CodEx: A modular framework for joint temporal de-blurring and tomographic reconstruction," IEEE Trans. Comput. Imaging **8**, 666–678 (2022).
8. B. Huyge, J. Renders, J. G. Sanctorum, *et al.*, "X-ray image reconstruction for continuous acquisitions with a generalized motion model," Opt. Express **32**(22), 39192–39207 (2024).
9. A. Olivo and R. Speller, "A coded-aperture technique allowing x-ray phase contrast imaging with conventional sources," Appl. Phys. Lett. **91**(7), 074106 (2007).
10. A. Olivo, "Edge-illumination x-ray phase-contrast imaging," J. Phys. Condens. Matter **33**(36), 363002 (2021).
11. A. Zamir, C. Hagen, P. C. Diemoz, *et al.*, "Recent advances in edge illumination x-ray phase-contrast tomography," J. Med. Imag **4**(04), 1 (2017).
12. G. Lioliou, O. Roche i Morgó, S. Marathe, *et al.*, "Cycloidal-spiral sampling for three-modal x-ray CT flyscans with two-dimensional phase sensitivity," Sci. Rep. **12**(1), 21336 (2022).
13. G. Lioliou, C. Navarrete-León, A. Astolfo, *et al.*, "A laboratory-based beam tracking X-ray imaging method achieving two-dimensional phase sensitivity and isotropic resolution with unidirectional undersampling," Sci. Rep. **13**(1), 8707 (2023).
14. C. Hagen, M. Endrizzi, R. Towns, *et al.*, "A preliminary investigation into the use of edge illumination X-ray phase contrast micro-CT for preclinical imaging," Mol. Imaging Biol. **22**(3), 539–548 (2020).
15. D. Shoukroun, A. Doherty, M. Endrizzi, *et al.*, "Post-acquisition mask misalignment correction for edge illumination X-ray phase contrast imaging," Rev. Sci. Instrum. **93**(5), 053706 (2022).
16. E. A. Zwanenburg, M. A. Williams, and J. M. Warnett, "Review of high-speed imaging with lab-based X-ray computed tomography," Meas. Sci. Technol. **33**(1), 012003 (2022).
17. F. Wali, S. Wang, H. Han, *et al.*, "Low-dose and fast grating-based X-ray phase-contrast imaging," Opt. Eng. **56**(09), 1 (2017).
18. G. B. Zan, H. J. Han, F. Wali, *et al.*, "Trimodal radiography using sinusoidal phase modulating grating interferometry," J. Appl. Phys. **126**(16), 164901 (2019).
19. J. Haeusele, C. Schmid, M. Viermetz, *et al.*, "Advanced phase-retrieval for stepping-free X-ray dark-field computed tomography," IEEE Trans. Med. Imaging **42**(10), 2876–2885 (2023).
20. M. Endrizzi, P. C. Diemoz, T. P. Millard, *et al.*, "Hard X-ray dark-field imaging with incoherent sample illumination," Appl. Phys. Lett. **104**(2), 024106 (2014).
21. M. Endrizzi, D. Basta, and A. Olivo, "Laboratory-based X-ray phase-contrast imaging with misaligned optical elements," Appl. Phys. Lett. **107**(12), 124103 (2015).
22. M. Endrizzi and A. Olivo, "Absorption, refraction and scattering retrieval with an edge-illumination-based imaging setup," J. Phys. D: Appl. Phys. **47**(50), 505102 (2014).
23. A. Zamir, M. Endrizzi, C. K. Hagen, *et al.*, "Robust phase retrieval for high resolution edge illumination X-ray phase-contrast computed tomography in non-ideal environments," Sci. Rep. **6**(1), 31197 (2016).
24. A. Doherty, S. Savvidis, C. Navarrete-León, *et al.*, "Edge-illumination X-ray dark-field tomography," Phys. Rev. Appl. **19**(5), 054042 (2023).
25. W. Yashiro and A. Momose, "Effects of unresolvable edges in grating-based X-ray differential phase imaging," Opt. Express **23**(7), 9233–9251 (2015).

26. F. Vittoria, M. Endrizzi, G. Kallon, *et al.*, "Beam tracking phase tomography with laboratory sources," J. Instrum. **13**(04), C04008 (2018).

27. L. C. Andrews, *Special functions of mathematics for engineers* (SPIE Press, 1998), chap. 3, p. 110

28. P. Modregger, T. P. Cremona, C. Benarafa, *et al.*, "Small angle X-ray scattering with edge-illumination," Sci. Rep. **6**(1), 30940 (2016).

29. P. Modregger, M. Endrizzi, and A. Olivo, "Direct access to the moments of scattering distributions in X-ray imaging," Appl. Phys. Lett. **113**(25), 254101 (2018).

30. J. Munkhammar, L. Mattsson, and J. Rydén, "Polynomial probability distribution estimation using the method of moments," PLoS One **12**(4), e0174573 (2017).

31. P. Modregger, M. Kagias, S. C. Irvine, *et al.*, "Interpretation and utility of the moments of small-angle X-ray scattering distributions," Phys. Rev. Lett. **118**(26), 265501 (2017).

32. B. Menke, "Moments of a convolution," https://www.ldeo.columbia.edu/menke/www_users_menke/research_notes/menke_research_note217.pdf (2020). Online. (Last accessed on 18/04/2025).

33. S. Jan, G. Santin, D. Strul, *et al.*, "GATE: a simulation toolkit for PET and SPECT," Phys. Med. Biol. **49**(19), 4543–4561 (2004).

34. S. Jan, D. Benoit, E. Becheva, *et al.*, "GATE V6: a major enhancement of the GATE simulation platform enabling modelling of CT and radiotherapy," Phys. Med. Biol. **56**(4), 881–901 (2011).

35. S. Agostinelli, J. Allison, K. Amako, *et al.*, "GEANT4–a simulation toolkit," Nucl. Instrum. Methods Phys. Res., Sect. A **506**(3), 250–303 (2003).

36. J. Sanctorum, J. De Beenhouwer, and J. Sijbers, "X-ray phase contrast simulation for grating-based interferometry using GATE," Opt. Express **28**(22), 33390–33412 (2020).

37. B. De Samber, J. Renders, T. Elberfeld, *et al.*, "FleXCT: a flexible X-ray CT scanner with 10 degrees of freedom," Opt. Express **29**(3), 3438–3457 (2021).

38. B. Huyge, P.-J. Vanthienen, N. Six, *et al.*, "Adapting an XCT-scanner to enable edge illumination X-ray phase contrast imaging," in *e-Journal of Nondestructive Testing*, vol. 28 2023.

39. T. P. Millard, M. Endrizzi, K. Ignatyev, *et al.*, "Method for automatization of the alignment of a laboratory based X-ray phase contrast edge illumination system," Rev. Sci. Instrum. **84**(8), 083702 (2013).

40. A. Doherty, L. Massimi, A. Olivo, *et al.*, "Optimal and automated mask alignment for use in edge illumination X-ray differential-phase and dark-field imaging techniques," Nucl. Instrum. Methods Phys. Res., Sect. A **984**, 164602 (2020).

41. K. W. Vugrin, L. P. Swiler, R. M. Roberts, *et al.*, "Confidence region estimation techniques for nonlinear regression in groundwater flow: Three case studies," Water Resour. Res. **43**(3), W03423 (2007).

42. C. K. Hagen, P. Coan, A. Bravin, *et al.*, "A continuous sampling scheme for edge illumination X-ray phase contrast imaging," J. Appl. Phys. **118**(5), 054901 (2015).

43. G. Lioliou, O. Roche i Morgó, A. Astolfo, *et al.*, "Recent developments in fly scan methods for phase and multi-contrast x-ray micro-CT based on amplitude modulated beams," Tomography of Materials and Structures **5**, 100034 (2024).